International Journal of Rock Mechanics & Mining Sciences 70 (2014) 286–295

Contents lists available at ScienceDirect

International Journal of Rock Mechanics & Mining Sciences

journal homepage: www.elsevier.com/locate/ijrmms

Experimental investigation of acoustic emissions and their moment tensors in rock during failure

Eyvind Aker [a,*], Daniela Kühn [b], Václav Vavryčuk [c], Magnus Soldal [a], Volker Oye [b]

[a] Norwegian Geotechnical Institute, Sognsveien 72, 0806 Oslo, Norway
[b] NORSAR, Gunnar Randers vei 15, 2007 Kjeller, Norway
[c] Institute of Geophysics, Academy of Sciences, Boční II/1401, Praha 4, 141 00 Praha, Czech Republic

ARTICLE INFO

Article history:
Received 29 November 2012
Received in revised form
13 February 2014
Accepted 4 May 2014

Keywords:
Acoustic emissions
Focal mechanisms
Moment tensors
Rock fracturing
Hoop stresses
Laboratory experiment

ABSTRACT

We study acoustic emissions (AEs) associated with shear and tensile failures around a horizontal borehole in a sandstone sample subjected to triaxial stress. The aim is to relate the AE event rate to macroscopic observations of sample deformation and the percentage of isotropic and deviatoric components of the seismic moment tensors to the expected failure mechanisms. The horizontal hole interferes with the applied load and forms a strongly spatially dependent anisotropic stress field, focusing the crack initiation into both shear and tensile failures. The recorded AEs follows reasonably well existing damage models, but the elastic solution of hoop stress does not represent the onset of failure around the borehole. The focal mechanisms correlate with the orientation of macroscopic fractures in the sample. Events close to the borehole show a higher fraction of isotropic percentage in moment tensors compared to events occurring in the macroscopic fracture featuring higher double-couple percentages. The inhomogeneous stress field due to the borehole and the stress induced damage is strongly affecting the axial and radial velocities which in turn affect the waveforms of the recorded AEs and the resulting moment tensors. The V_P/V_S ratio obtained from the ratio of isotropic to compensated linear vector dipole components of the moment tensors is close to that obtained from ultrasonic velocity measurements.

1. Introduction

Acoustic emissions (AEs) are elastic waves generated spontaneously from the creation of micro-cracks (micro-fractures) when a rock is subjected to sufficiently high load. The AE waveforms feature remarkable similarities with earthquakes and thus, recording and analyzing them may improve understanding of a wide range of fracture processes [1]. So far, the failure processes have been studied by AEs in various types of rocks, concretes and in engineered materials finding applications in material science as well as in geosciences (*e.g.* [2]). Often cited is the classical work by Lockner et al. [3], studying fracture propagation in granite using AEs as feedback control to the loading system to slow down the macroscopic failure of the sample. More recently, AEs have been used to study fracturing due to fluid injection and pore pressure changes [4,5], the formation of compaction bands [6,7], the evolution of borehole breakouts [8], and the creation of fractures under polyaxial stress conditions [9].

The aim of the paper is to study a variety of source mechanisms of AE events associated with crack initiation, coalescence and macroscopic failure of a rock sample subjected to increasing load and forming complex stress conditions. The sample is loaded in a triaxial apparatus where AE waveforms and macroscopic parameters like stress, strain and acoustic velocities are recorded. The sample contains a small cylindrical hole to simulate a situation observed *in situ* in boreholes (*e.g.*, during hydrocarbon production, subsurface waste or CO_2 injection) and in mining seismology (*e.g.*, stress accumulation close to tunnels and shafts). The cylindrical hole interferes with the applied load and forms a strongly spatially dependent anisotropic stress field focusing the crack initiation into shear and tensile failures.

A detailed spatio-temporal evolution of the AE activity is monitored from the very beginning of loading to the final stage of creating a major fracture in the sample. The AE events are located and compared to the macroscopic failure planes using an X-ray CT scanner. The AE event rate is related to macroscopic stress and strain behavior using existing damage models. Full waveforms of AEs are investigated to calculate source mechanisms and seismic moment tensors which proved to be a useful tool for quantitative characterization of source mechanisms of AEs [1,10–14]. In contrast to standard fault-plane solutions assuming

* Correspondence to: AGR Petroleum Services, Karenslyst allé 4, 0213 Oslo, Norway. Tel.: +47 47 90 77 02.
E-mail address: eyvind.aker@agr.com (E. Aker).

http://dx.doi.org/10.1016/j.ijrmms.2014.05.003
1365-1609/

pure shear fracturing, moment tensors take into account volumetric components of the source as well as combinations of shear with tensile or compressive motions [15,16] and can thus be used for interpreting a non-reversible decrease or increase of rock volume during uniaxial or triaxial laboratory experiments on rock specimens [*e.g.* 17,18]. The moment tensors were computed for a subset of recorded events and associated with the expected failure mechanisms around the borehole. We also discuss how the anisotropic stress field influences the macroscopic velocities and the resulting moment tensors. Finally, we estimate the ratio of compressional to shear velocity (V_P/V_S) using the ratio of isotropic (ISO) to compensated linear vector dipole (CLVD) components of the moment tensors and compare it to the velocity measurements.

2. The experimental setup

The experimental setup consists of a rock sample mounted inside a triaxial apparatus controlling the axial (vertical) stress (σ_1), the radial (horizontal) confining pressure (σ_3) and the pore pressure of the fluid inside the rock (Fig. 1a). A detailed description of the triaxial cell is provided in [19].

The rock sample is a 50.8 mm diameter and 127 mm long cylindrical specimen of Vosges sandstone [20] with porosity around 21% and uniaxial compressive strength of 48 MPa. The rock sample is weakly layered horizontally, thus static and dynamic elastic parameters display transversely isotropic symmetry. A small cylindrical hole (borehole) of 5.2 mm diameter is drilled horizontally at mid-height through the sample (Fig. 1b). The sample (denoted T1790) is put between a top- and bottom pedestal containing inlet and outlet for pore fluid. The sample under investigation was dry; hence the pore pressure was the ambient pressure. The bottom pedestal is fixed while the top pedestal is moving vertically downward at a specific strain rate. The axial strain of the sample is monitored by two LVDTs that are mounted to the top- and bottom pedestals. The radial strain is measured using a cantilever supplied with strain gauges and measuring pins that are in direct contact with the sample. The axial load is controlled by an external force actuator and the confining pressure is controlled by a GDS pump.

The AEs are monitored by an array of twelve piezoelectric receivers (pinducers) positioned at the surface of the sample and recording the waveforms by a data acquisition system; see also [21]. The pinducers are sensitive to particle displacements normal to the surface of the sample favoring the detection of normal incident compressional P waves. They are negatively polarized defined as the negative voltage that is produced when a compressional P wave hits the surface of the pinducer. The waveforms are recorded at 10 MHz sampling rate at 12-bit resolution. A band-pass filter with 50 kHz low-cut and 1.5 MHz high-cut frequency was applied to the data to remove noise before further processing. The resonance frequency of the pinducers is about 1 MHz and most of the energy in the signal is centered on 0.5 MHz.

A nitrile rubber sleeve is used to isolate the sample from the confining oil and fix the positions of the pinducers. Ultrasonic compressional (P) and shear (S) wave velocities of the rock are measured along the axial and the radial directions using piezoelectric transducers that are mounted inside the top- and bottom pedestals (axial direction) and to the rubber membrane (radial direction). The position of the pinducers and the transducers relative to the surface of the cylindrical rock is shown in Fig. 1c. The velocities are measured at regular intervals during the course of the experiment, and are input to the event location algorithm computing the source positions of the recorded AEs. The recording system and software are manufactured by Applied Seismology Consultants and the rubber sleeve, cantilever and the piezoceramic receivers/transducers are manufactured by Ergotech Ltd.

The relative sensitivity of each pinducer was measured prior to the experiment by recording the signal amplitudes on the pinducers when transmitting P waves through an aluminum cylinder. The aluminum cylinder, pinducers and transducers were mounted in the rubber sleeve and loaded to 5 MPa isotropic pressures. The top and bottom P-wave transducers were used to generate an acoustic pulse that was recorded by the pinducers. The relative

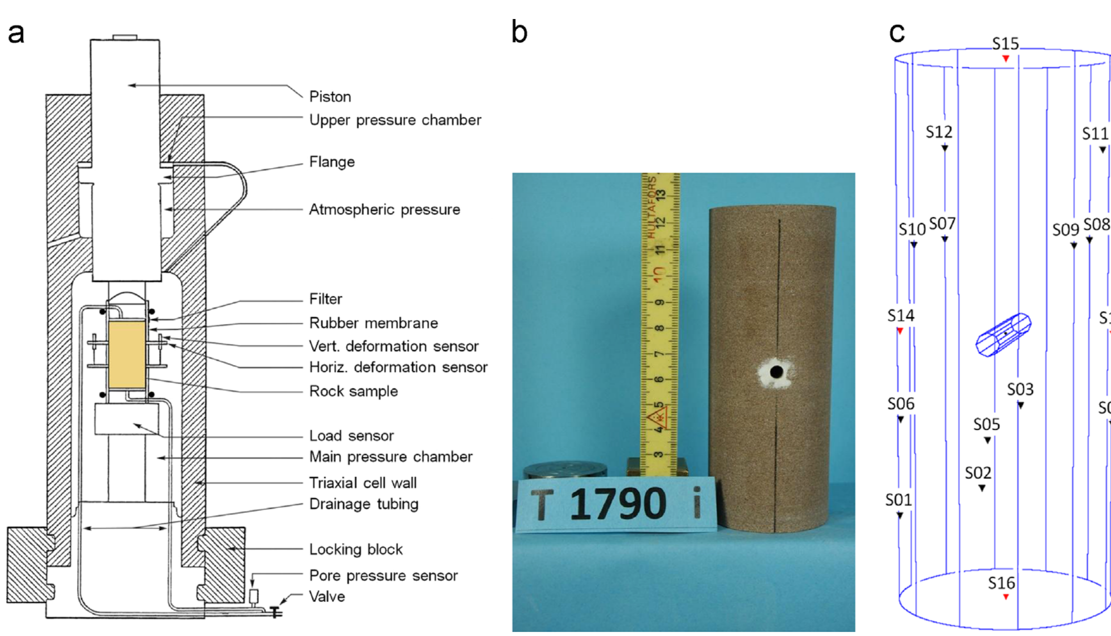

Fig. 1. (a) The principle of the triaxial apparatus. (b) The test specimen is a cylindrical sandstone core from the Vosges Mountains in France, containing a 5.2 mm diameter central borehole. A thin layer of gypsum (white area) is applied on the surface to obtain a perfect cylindrical shape around the borehole. (c) A sketch of the sample with the horizontal borehole in the middle and 12 pinducers positioned at the surface (black triangles, S01–S12). Transducers for measuring the P- and S-wave velocities are indicated with red triangles (S13–S16). (For interpretation of the references to color in this figure legend, the reader is referred to the web version of this article.)

sensitivity of the pinducers was defined as the relative amplitude of the first phase after compensating the amplitude for source-receiver distance. These relative sensitivity values were used when later computing moment tensors of the AE sources (after Pettitt [14]). The absolute sensitivity of the transducers has not been measured and therefore the seismic moment reported here is a relative measure.

3. Relating AEs to macroscopic deformation and failure

The sample was first loaded isotropically to $\sigma_1=\sigma_3=10$ MPa. Then the deviatoric stress $(\sigma_1-\sigma_3)$ was increased until failure of the sample while keeping the confining stress constant. The maximum vertical stress before macroscopic failure was 76.3 MPa. The AE activity was monitored when $\sigma_1-\sigma_3>0$ (shearing phase) until post-failure of the sample. In total, more than 33,000 hits (*i.e.*, a voltage signals recorded by a receiver being above a pre-defined threshold value) were registered on individual receivers. An AE event constitutes a set of hits that triggered three or more receivers within a small time window. The hits were grouped into AE events and their full waveforms were recorded with length of the 102.4 μs. The data acquisition system captured 2551 AE events.

Fig. 2 shows the stress–strain curves and the rate of AEs for increasing deviatoric stress. The recorded event rate at peak stress is about 250 events per minute followed by a peak in event rate of 550 during shearing on the failure plane. The estimated event rate is based on the 2551 recorded events with waveforms. The stress–strain curve can be divided into six phases corresponding to [22]: i) micro-crack closure and stiffening of the sample; ii) linear elastic behavior; iii) initiation of dilatancy and non-linear behavior; iv) localization of deformation during hardening; v) peak strength and macroscopic failure; and vi) residual behavior. In the figure, the deviatoric stress–axial strain curve is reasonably matched up to peak with a damage model based on AEs [23]. The model assumes isotropic damage from open cracks and a crack density proportional to the number of AEs giving:

$$\sigma_1-\sigma_3=\frac{\varepsilon_1 E_0}{1+kN_{AE}} \tag{1}$$

where E_0 is the initial elastic modulus, k is a constant, and N_{AE} is the number of AEs and ε_1 the axial strain. In Fig. 2, the curve fit is obtained using $E_0=12$ GPa and $k=10^{-4}$.

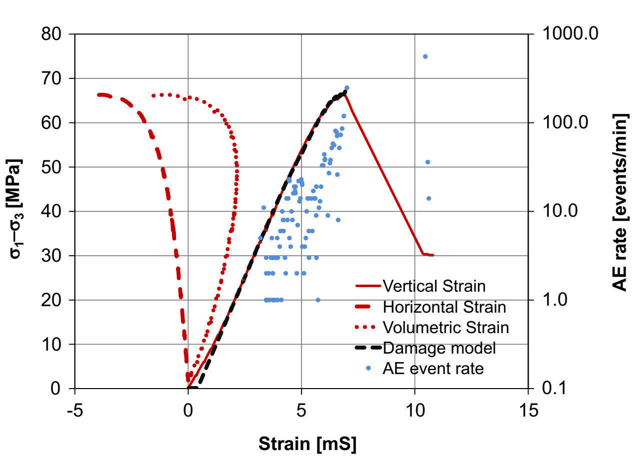

Fig. 2. Deviatoric stress $(\sigma_1-\sigma_3)$ *versus* vertical (axial), horizontal and volumetric strains for T1790 (red solid, dashed and stippled lines). Also shown is the recorded AE event rate (blue points) plotted *versus* vertical strain. Black stippled line shows the predicted stress–strain behavior using the damage model based on AEs. (For interpretation of the references to color in this figure legend, the reader is referred to the web version of this article.)

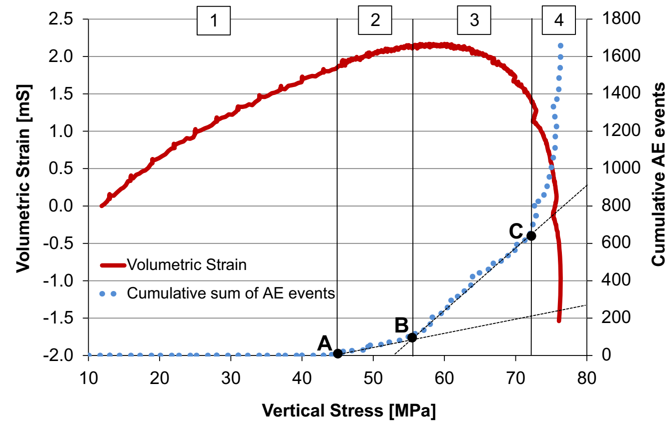

Fig. 3. Volumetric strain and cumulative number of AE events *versus* vertical stress for T1790. During measurement of P- and S-wave velocities (approximately every 3 MPa) loading is paused while AE events still continue, which results in saw teeth on the AE curve. The behavior can be divided into four phases indicated by the numbers above the panel; see text for details.

Fig. 3 shows the volumetric strain (positive means contraction) and cumulative number of AEs as a function of the vertical stress applied up to peak strength. Four stages of AEs are clearly seen: before point A, no AEs are detected. After a first phase of slow linear increase (A to B), the cumulative number of AEs increase sharply until point C, where an accelerated phase of AEs starts. Intuitively, we expect that the first phase of AEs is related to development of borehole breakouts in a global contracting behavior of the sample. Phases B to C corresponds to the localization of macroscopic shear bands associated with dilatancy of the sample. The last phase, initiated from point C (before peak stress), leads to catastrophic failure of the sample. These stages will be referred to as phases 1 to 4 in the following.

Based on the Kirsch elastic stress concentration [24], the onset of shear failure at the unsupported borehole wall is expected when the hoop stress is equal to the uniaxial compressive strength (UCS) of the rock, giving a vertical stress equal to $(10+48)/3=19$ MPa. The first AE is recorded for a vertical stress equal to 43 MPa (point A, Fig. 3), indicating that the elastic solution may not be representative for the stress concentrations around the borehole. The effect of scale on the strength of boreholes is well known in the literature. For example, Dresen et al. [8] indicated that the critical hoop stress for nucleation of borehole breakouts exceeds 2.5 times the uniaxial compressive strength for borehole diameters less than 20 mm. Experiment T1790 gives a ratio equal to 2.5, on the lower range of the values reported in [8]. However, in our case, the borehole is subjected to large stress anisotropy during loading.

The sample was imaged post-test using an X-ray micro-computed tomography scanner (Nikon Metrology XT H 225 LC industrial type with a 225 kV micro-focus X-ray source, minimum 3 μm focal spot size) to map the internal damage and the macroscopic failure plane. The processed images are shown in Fig. 4 and clearly display the macroscopic failure plane (Fig. 4a) and debris that have fallen into the horizontal hole (Fig. 4c).

4. Effect of rock damage and stresses on acoustic velocities

The ultrasonic P- and S-wave velocities in the axial and radial directions were measured at intervals of 1 MPa between 3 and 10 MPa of the isotropic horizontal stress, and at intervals of 3 MPa from 10 to 76 MPa of the vertical stress. S-wave velocities were measured for two polarization directions. In the vertical direction, the polarization of the S wave was normal and parallel to the

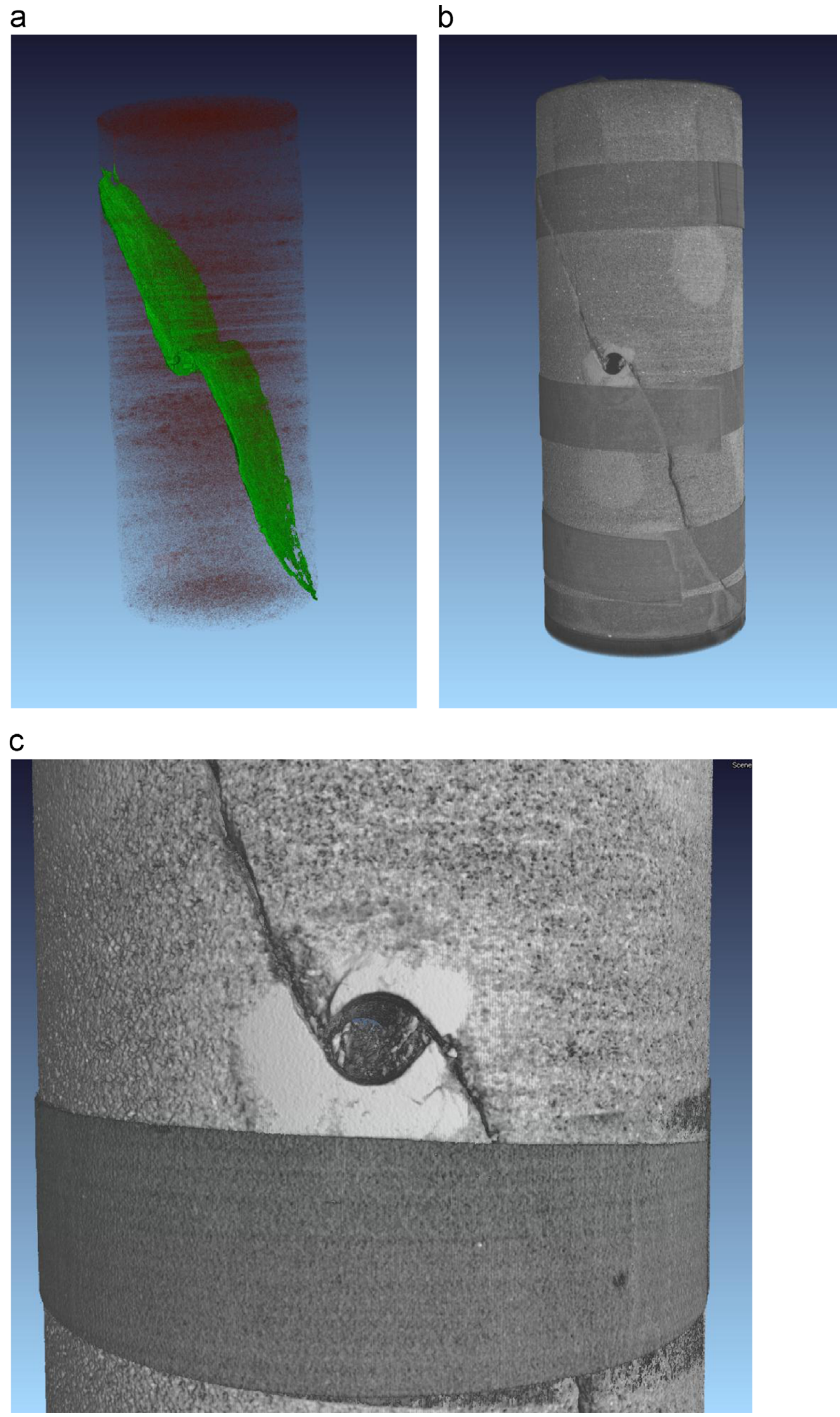

Fig. 4. 3D high-resolution X-ray CT scan of the sample after testing. (a) Pore volume (red), fractured volume (green), (b) surface of the whole sample, and (c) close up of the horizontal hole. Note debris inside the hole. (For interpretation of the references to color in this figure legend, the reader is referred to the web version of this article.)

borehole axis denoted as V_{S1} and V_{S2}, respectively. In the horizontal direction, the polarization was normal and parallel to the bedding plane (*i.e.* the horizontal plane) denoted as V_{SV} and V_{SH}, respectively (see Fig. 5a for details). The vertical and horizontal P-wave velocity (V_{P0} and V_{P90}) and the horizontal S-wave velocity of the two polarizations (V_{SV} and V_{SH}) are plotted in Fig. 5b. The ratio of V_{P0} to V_{P90} is about 0.88 while the ratio of V_{SV} to V_{SH} is about 0.92 at 10 MPa of the isotropic stress. Thus, the sample complies with transversely isotropic symmetry along the vertical axis.

When increasing the deviatoric stresses ($\sigma_1 - \sigma_3 > 0$), the P- and S-wave velocities in vertical and horizontal directions are affected by the induced stress field and by the creation of micro-fractures. Velocity V_{P0} increases with the vertical stress due to the stiffening of the grain–grain contacts, while V_{P90} decreases and becomes less than V_{P0} as the sample gets closer to failure (Fig. 5b, refer also to phases 3 and 4 in Fig. 3). Similar behavior is observed for V_{SV} and V_{SH} where V_{SH} becomes less than V_{SV} at about $\sigma_1 = 55$ MPa, coinciding with the progressive growth of shear bands associated with sample dilatancy (refer to point B in

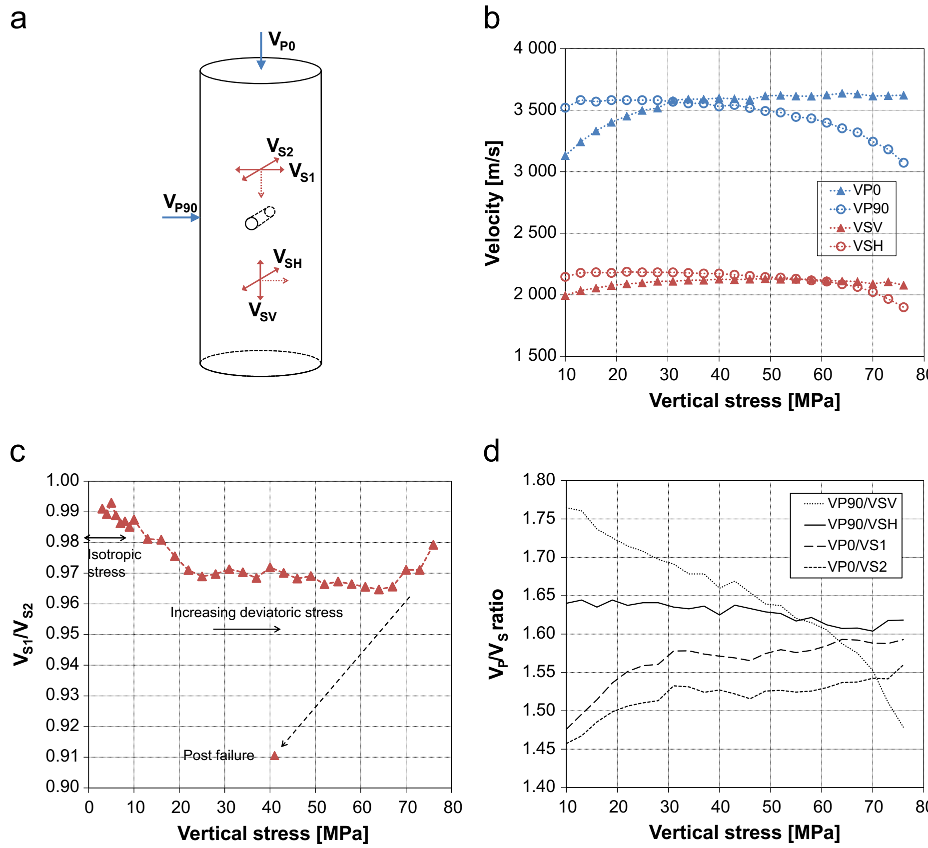

Fig. 5. (a) The orientation and polarization of the different P- and S-wave velocities that were measured with ultrasonic transducers. (b) Ultrasonic P-wave velocities in the vertical (V_{P0}) and horizontal (V_{P90}) directions, and horizontal S-wave velocities polarized in the vertical (V_{SV}) and horizontal (V_{SH}) directions as a function of vertical stress. (c) The ratio of vertical S-wave velocity polarized normal to the borehole axis (V_{S1}) and the vertical S-wave velocity polarized parallel to the borehole axis (V_{S2}) as a function of vertical stress. Under isotropic stresses, the ratio is close to 1 as expected, while the borehole induces stress anisotropy lowering the V_{S1}/V_{S2} ratio at increasing deviatoric stresses. (d) V_P/V_S ratios for the different combinations of vertical and horizontal P and S waves as a function of vertical stress.

Fig. 3). Fig. 5b supports the assumption that the deviatoric stresses favor creation of vertical micro-fractures causing a reduction in V_{P90} and V_{SH} relative to V_{P0} and V_{SV}. We also notice that the ratio of V_{S1} to V_{S2} (in the vertical direction) decreases slightly with increasing deviatoric stresses (Fig. 5c). Thus, the S wave polarized parallel to the borehole axis becomes a few percent faster than the one polarized normal to the borehole axis probably due to stress induced anisotropy and damage close to the borehole.

The effect of the borehole on the internal stresses was investigated by simulating the rock deformation by a geomechanical finite element code. The internal deviatoric stresses are displayed in Fig. 6 at $\sigma_1-\sigma_3=55$ MPa (corresponding to phase 3 in Fig. 3). The borehole causes the deviatoric forces to concentrate in a wing like pattern favoring vertically oriented micro-fractures along the borehole axis in accordance to the observed stress dependency of P- and S-wave velocities.

Because of the stress concentration around the borehole it is difficult to estimate a consistent ratio of P- to S-wave velocities (V_P/V_S ratio) for the entire sample. This is illustrated in Fig. 5d plotting the V_P/V_S ratio for the different combinations in the vertical and the horizontal directions. The sample starts to dilate at about $\sigma_1=55$ MPa (point B in Fig. 3); the V_P/V_S ratio in the horizontal direction is about 1.62. In the vertical direction, the V_P/V_S ratio is between 1.52 and 1.58 depending on which of the S waves (S1 or S2) is considered. Closer to failure, the V_P/V_S ratio is about 1.55–1.60. In the following section we will compute moment tensors of selected events and obtain the V_P/V_S ratio by applying the model of tensile fracturing [15,16].

5. Source locations and moment tensor inversion

The InSite software package [25] based on the so-called collapsing grid search algorithm was applied for the event location. The locations are computed by minimizing the residuals of the P-wave arrival times. The velocity model is obtained from measurements on the sample being approximated by homogeneous and transversely isotropic medium. In total, 1072 events that triggered a minimum of six receivers were located. A subset of 305 events that triggered a minimum of 10 receivers are shown in Fig. 7a overlaid on a cross-sectional X-ray CT image. The event locations match well the macroscopic fractures developed during the experiment. Of these events, 162 were considered having sufficiently high quality for moment tensor inversion (see details below) and is plotted in Fig. 7b and c. In Fig. 7b the events are colored according to their origin time. First, the events occur near to the borehole; later, the events concentrate near the developing macroscopic fractures on both sides of the borehole (later referred to as fracture wings A and B).

Events in both additional wings not developing into a macroseismic fracture occur at the same time as events close to the borehole. In Fig. 7c, events are colored according to the different phases of the experiment as described in Section 3 and illustrated in Fig. 3 (green: phase 2, blue: phase 3, red: phase 4).

In order to compute moment tensors, the pinducers were calibrated (see Section 2) and the recorded amplitudes were corrected. In addition, we assume a cosine sensitivity function for the sensor directivity (*i.e.*, the sensitivity of amplitudes of

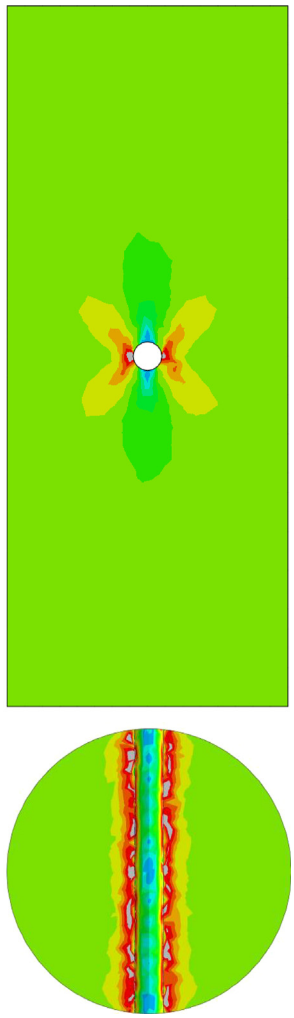

Fig. 6. Simulated internal deviatoric stress due to the presence of borehole, at $\sigma_1-\sigma_3=55$ MPa. Colors correspond to the internal deviatoric stresses; red is highest (90 MPa) and blue is lowest (0 MPa). The upper panel displays a longitudinal cross section and the lower panel displays a horizontal cross section through the center of the borehole. (For interpretation of the references to color in this figure legend, the reader is referred to the web version of this article.)

waves arriving at different incidence angles) exhibiting the highest sensitivity for the normal incidence. Example waveforms are displayed in Fig. 8 for an event close to the borehole and for an event situated in one of the macroscopic fracture wings. In both cases, no S wave can be distinguished due to the proximity of the source and receivers. The waveforms are complex and characterized by long coda waves produced by interaction of emitted waves with the surface of the borehole or with the specimen's walls. In order to suppress the effects of wave propagation on the moment tensor inversion, we perform an inversion of P-wave first-onset amplitudes. The signal-to-noise ratio was not sufficiently high enough at all receivers to allow for picking the P-wave amplitudes reliably. Therefore, we selected a subset of 162 high-quality events, for which the P-wave first onset amplitudes were picked manually with sufficient quality at minimum of six receivers and with good focal sphere coverage. The maximum azimuthal gap was 135° and the maximum take-off angle gap was 60°. The moment tensors were calculated using the amplitude inversion in time domain (see [26, eq. (3.23)]). The ray-theoretical P-wave amplitudes of the Green's function were calculated assuming a homogeneous velocity model. The time-dependence of the source-time function was neglected [27,28]. The time-independent moment tensors were computed using a generalized linear inversion [29].

The results of the moment tensor inversion are shown in the Hudson T–k plot in Fig. 9. Fig. 9a displays the Hudson plot subdividing the coordinate space into different source mechanisms. Fig. 9b–d displays the solutions for all 162 events colored according to their distance from the borehole, their origin time, and their seismic moment. The seismic moments of the analyzed events as well as their double-couple percentages increase in time (and thus with increasing the deviatoric stress); the isotropic components decrease in time. The majority of events are situated in the upper half of the Hudson plot indicating a tendency of fractures to be opened. We observe that events with small seismic moments are related to more tensile mechanisms, whereas events having large seismic moments are close to pure shear mechanisms. Similar observations (tensile micro-cracks in early stages of loading, localized shear fracturing at later stages) were also reported in [1,12,30–32]. Such behavior is expected for materials having a low porosity and no pre-existing cracks [1].

Fig. 10 shows the decomposition of moment tensors into isotropic (red), double-couple (blue) and compensated linear vector dipole (green) parts for events close to the borehole (left) and within the fracture wings (right). Although the distribution of the percentages is irregular, events occurring close to the borehole show a higher fraction of isotropic percentage compared to events occurring within the fracture wings mostly featuring a higher fraction of DC percentages. (For interpretation of the references to color in this figure, the reader is referred to the web version of this article.)

Fig. 11 displays event locations colored according to their distance from the borehole (middle plot) and the double-couple and non-double-couple components of events occurring in the fracture wings A (left-hand plots) and fracture wing B (right-hand plots). The arrows highlight the strike direction of the borehole. The lower left and right plots illustrate the P (compressional) and T (tensional) axes calculated from eigenvectors of the moment tensors. The plots indicate that the source mechanisms basically coincide with the orientation of the fractures in the sample. One of the nodal lines has a strike close to the strike of the hole. The fractures are almost vertical, so the focal mechanisms are close to normal/reverse faulting. The P and T axes are more strongly clustered for fracture wing B than wing A, most likely because the events in wing B are situated at larger distances from the hole and therefore the waveforms are less affected by the borehole. On the other hand, the focal mechanisms in wing A are more scattered due to the more complex stress conditions close to the borehole (see Fig. 6) and due to the interaction of the wave field with the borehole. The events of both wings display significant non-double-couple components. The isotropic (ISO) and compensated linear vector dipole (CLVD) components have positive values as illustrated in the upper left and right plots. This indicates tensile fracturing, which is predicted also by the stress and velocity analysis. Applying the model of tensile fracturing [15], the P- to S-wave velocity ratio can be retrieved employing a linear regression (see dashed lines in Fig. 11, left and right top plots) attaining a realistic value of $V_P/V_S=1.73$. For a comparison, the V_P/V_S ratio determined from velocity measurements in the axial and radial directions close to failure is about 1.55–1.60 (see Fig. 5d) being reasonably close to the obtained value in Fig. 11.

When interpreting the focal mechanisms and particularly the non-double-couple components of the moment tensors, we have to keep in mind that the moment tensor solutions have a limited accuracy. The errors of the moment tensors can be produced by noise and limited amount of data and by various approximations made during the inversion. For example, the applied Green's functions may not describe the medium appropriately, because we omit anisotropy of the specimen during the inversion (see Section 4). In addition, the coupling effects between the sensors and the

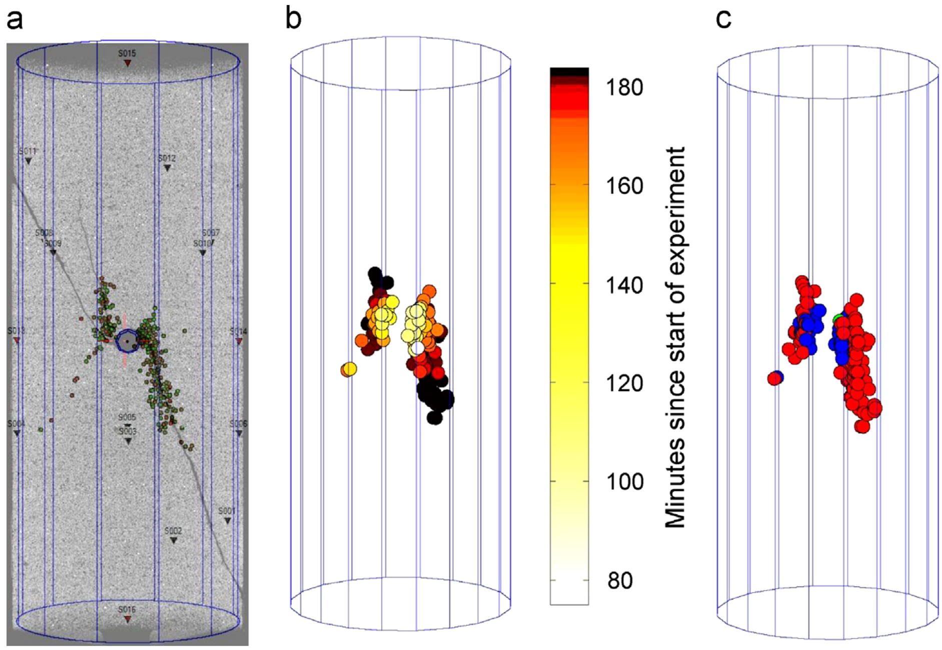

Fig. 7. Location of events. (a) Locations of 305 events overlaid on a 2D longitudinal cross sectional cut of the 3D X-ray CT image. The color scale of the events represents the relative amplitude defined as the logarithm of the sum of the waveform root-mean-square (RMS) amplitudes multiplied by the source-receiver distance. (b) 162 events selected for moment tensor inversion, colored according to origin time in minutes after start of the experiment. (c) The same events as shown in panel (b) colored according to the phase of the experiment, green: phase 2, blue: phase 3, and red: phase 4. (For interpretation of the references to color in this figure legend, the reader is referred to the web version of this article.)

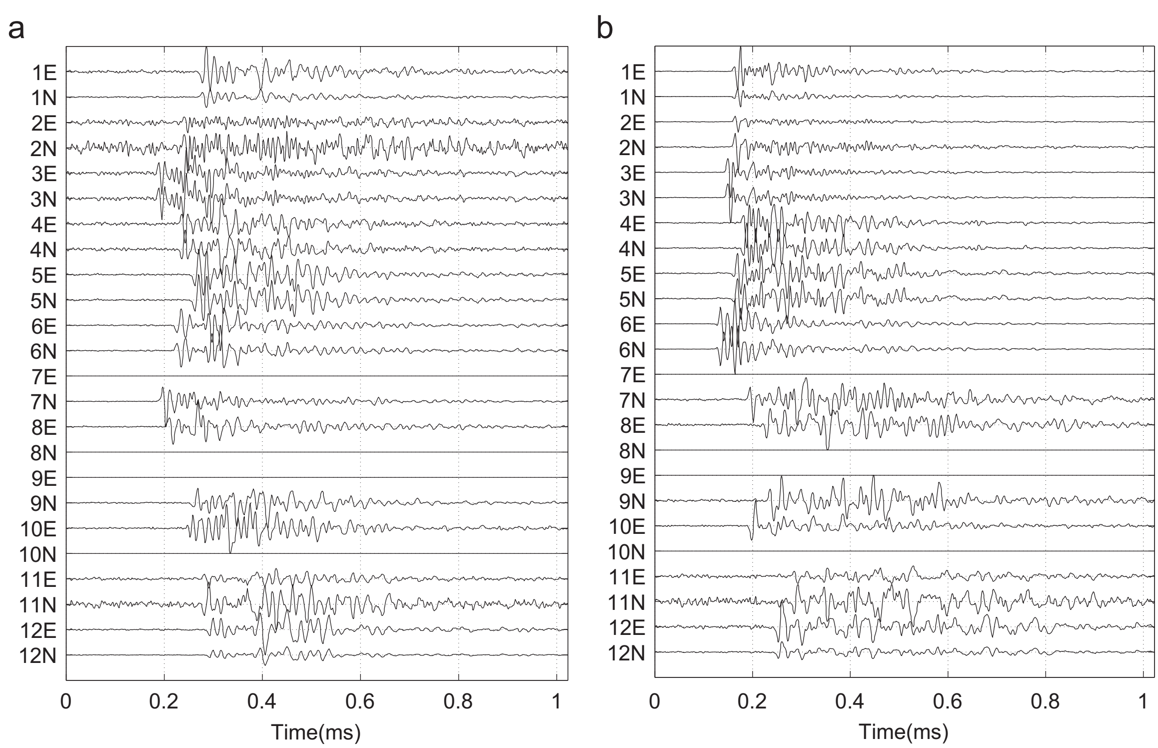

Fig. 8. Example seismograms for an event close to the borehole (left) and located in the fracture wing (right). Traces recorded by pinducers are split into East and North component.

rock specimen during the experiment were disregarded when assessing the relative pinducer sensitivities. Inaccuracies in event locations produce errors of the moment tensor solutions. Finally, the P-wave first-onset amplitudes may contain noise and may partly be distorted by reflected or scattered waves arriving immediately after the direct P wave.

6. Conclusions

In this paper, the results of a triaxial experiment carried out to investigate the source mechanisms of AE events during loading of a perforated sandstone sample have been presented. The decomposition of the moment tensors associated with the recorded

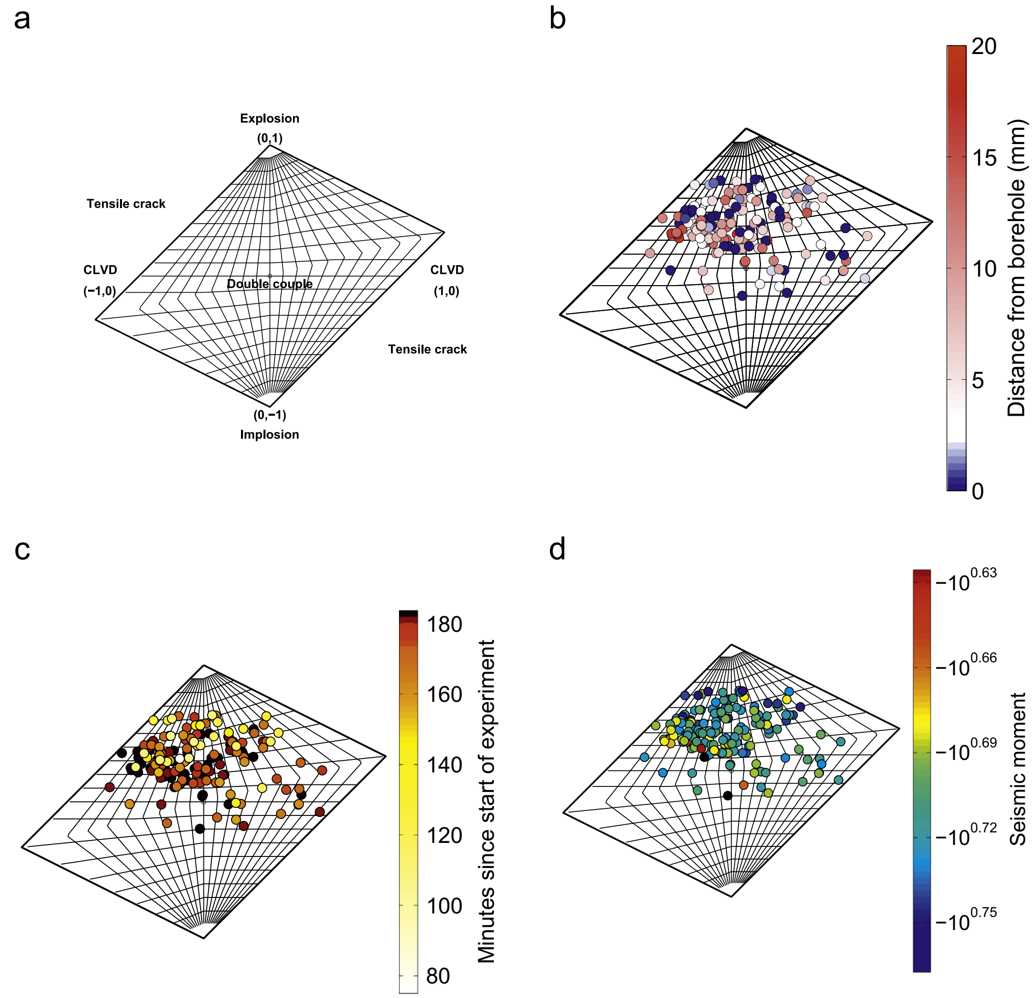

Fig. 9. Hudson diagrams of the events. Top left: interpretation of T–k coordinates; top right: T–k plot of 162 events colored according to distance from the borehole in meters; bottom left: T–k plot of 162 events colored according to origin time in minutes since start of the experiment; bottom right: T–k plot of 162 events colored according to relative seismic moment (largest two events plotted in black in order to render the color scale more meaningful).

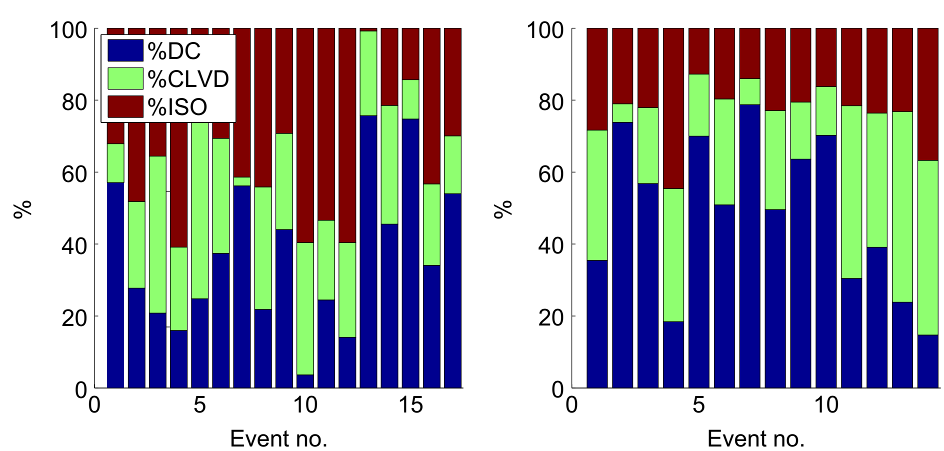

Fig. 10. Decomposition of moment tensors into ISO, CLVD and DC percentages; left: mechanisms of events close to the borehole, right: mechanisms of events located in the fracture wings. The percentages of the ISO, CLVD and DC are calculated according to [15].

events shows the complexity of fracture mechanisms during failure, *i.e.* mixed mode of tension and shear components. The locations of the AE events correlate well with the X-ray CT images taken post-test. The observed AE event rate is divided into four phases with increasing number of AEs: pure elastic phase, development of borehole breakouts, localization of macroscopic shear bands, and catastrophic failure. Recorded AEs follow reasonably well existing damage models but the elastic solution of the hoop stress does not represent the onset of failure around the borehole. One of the nodal planes calculated from the moment

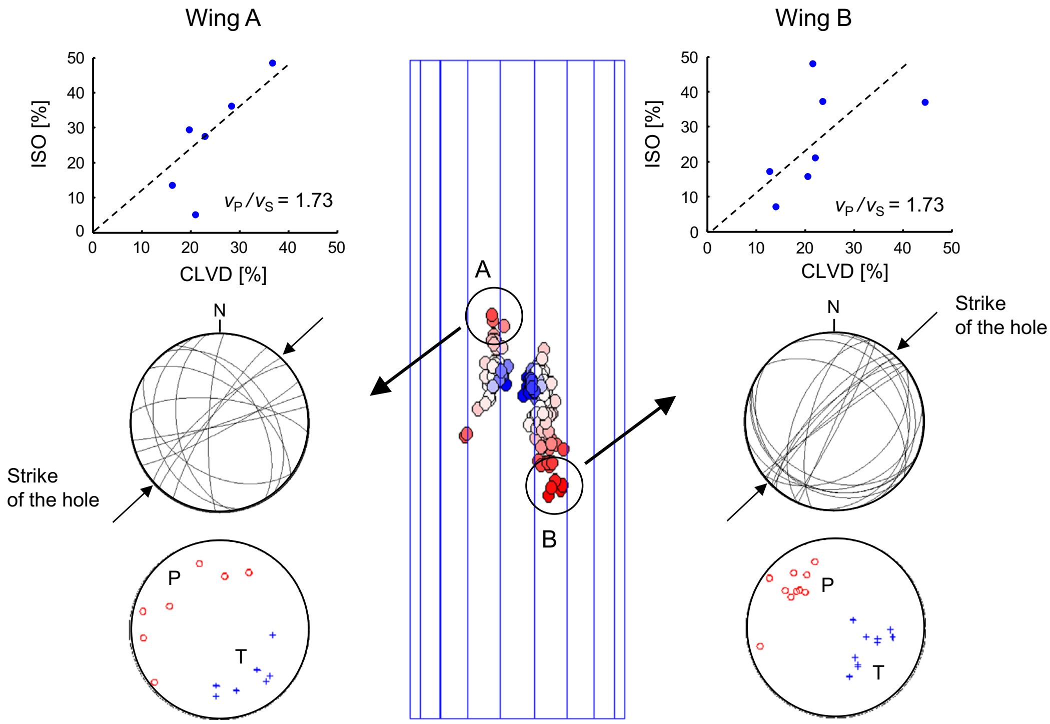

Fig. 11. Fault plane solutions for selected events; middle: locations of events, colored according to distance from the borehole; left: results for events situated in wing A (from top to bottom: CLVD-ISO plot, fault plane solutions, *P* and *T* axes); right: the same for events situated in wing B. The percentages of the ISO, CLVD and DC are calculated according to [15].

tensors coincides with the orientation of the macroscopic fractures in the sample. Events close to the borehole show a higher fraction of isotropic percentage compared to the events occurring in the macroscopic fracture featuring higher fraction of the DC percentage. Analysis of axial and radial P- and S-wave velocities together with modeling of internal stresses highlight the effects of stress induced damage and the influence of the borehole on the measured P- and S-wave velocities. As a result is it difficult to estimate a consistent V_P/V_S ratio for the entire sample. Despite this, the ratio obtained from the ISO and CLVD cross plots using the model of tensile fracturing [16] is close to values obtained from the ultrasonic measurements. Since the waveforms are affected strongly by the presence of the horizontal borehole and probably also by the specimen's walls, the moment tensors computed from the P-wave first-onset amplitudes are not highly accurate. To improve their accuracy, a full waveform inversion should be applied using Green's functions computed for the actual geometry of the sample including the borehole. In general, events located in the vicinity of the borehole display complex focal mechanisms because of the complex stress field.

Acknowledgments

We thank Will Pettitt for his review. The work was funded by the ACUPS Project (financed by the Norwegian Research Council and industry partners BP, Statoil and Total; Grant no. 176016), Grant Agency of the Czech Republic, Grant no. P210/12/1491, and by the European Community's FP7 Consortium Project AIM “Advanced Industrial Microseismic Monitoring”, Grant agreement no. 230669. Support from these organizations is greatly acknowledged. Contributions and comments from Huynh Dat Vu Khoa, Hom Nath Gharti and Fabrice Cuisiat (post-mortem) are greatly appreciated.

References

[1] Graham CC, Stanchits S, Main IG, Dresen G. Comparison of polarity and moment tensor inversion methods for source analysis of acoustic emission data. Int J Rock Mech Min Sci 2010;47:161–9.
[2] Michlmayr G, Denis C, Dani O. Sources and characteristics of acoustic emissions from mechanically stressed geologic granular media—a review. Earth Sci Rev 2012;112:97–114.
[3] Lockner DA, Madden TR. Quasi-static failure growth and shear fracture energy in granite. Nature 1991;350:39–42.
[4] Stanchits S, Mayr S, Shapiro S, Dresen G. Fracturing of porous rock induced by fluid injection. Tectonophysics 2011;503:129–45.
[5] Mayr SI, Stanchits S, Langenbruch C, Dresen G, Shapiro SA. Acoustic emission induced by pore-pressure changes in sandstone samples. Geophysics 2011;76: MA21–MA32.
[6] Fortin J, Stanchits S, Dresen G, Gueguen Y. Acoustic emission and velocities associated with the formation of compaction bands in sandstone. J Geophys Res 2006;111(B10):B10203.
[7] Townend E, Thompson BD, Benson PM, Meredith PG, Baud P, Young RP. Imaging compaction band propagation in Diemelstadt sandstone using acoustic emission locations. Geophys Res Lett 2008;35:L15301.
[8] Dresen G, Stanchits S, Rybacki E. Borehole breakout evolution through acoustic emission location analysis. Int J Rock Mech Min Sci 2010;47:426–35.
[9] King MS, Pettitt WS, Haycox JR, Young RP. Acoustic emissions associated with the formation of fracture sets in sandstone under polyaxial stress conditions. Geophys Prospect 2012;60:93–102.
[10] Dahm T, Manthei G, Eisenblätter J. Relative moment tensors of thermally induced microcracks in salt rock. Tectonophysics 1998;289:61–74.
[11] Ohtsu M. Moment tensor analysis of AE and SiGMA code. In: Kishi T, Ohtsu M, Yuyama S, editors. Acoustic emission—beyond the millenium. Amsterdam: Elsevier; 2000. p. 19–34.
[12] Chang SH, Lee CI. Estimation of cracking and damage mechanisms in rock under triaxial compression by moment tensor analysis of acoustic emission. Int J Rock Mech Min Sci 2004;41:1069–86.
[13] Manthei G. Characterization of acoustic emission sources in a rock salt specimen under triaxial compression. Bull Seismol Soc Am 2005;95(5):1674–700.
[14] Pettitt WS. Acoustic emission source studies of microcracking in rock [Ph.D. thesis]. UK: Keele University; 1998.
[15] Vavryčuk V. Inversion for parameters of tensile earthquakes. J Geophys Res 2001;106(B8):16.339–55.
[16] Vavryčuk V. Tensile earthquakes: theory, modeling and inversion. J Geophys Res 2011;116(B12):320.
[17] Brace WF, Paulding BW, Scholz C. Dilatancy in the fracture of crystalline rocks. J Geophys Res 1966;71:3939–53.

[18] Miller AD, Julian BR, Foulger GR. Non-double-couple earthquakes. 2. Observations. Rev Geophys 1998;133:309–25.
[19] Berre T. Triaxial testing of soft rocks. Geotech Test J 2011;34:61–75.
[20] Bésuelle P. Déformation et rupture dans les roches tendres et les sols indurés: comportement homogène et localization [Ph.D. thesis].Grenoble, France: Université de Grenoble I; 1999.
[21] Aker E, Cuisiat F, Soldal M, Kühn D. Relating acoustic emission sources to rock failure around a borehole. In: Proceedings of the 72nd EAGE conference & exhibition. Barcelona; 2010. p. 569.
[22] Wawersick WR, Fairhurst C. A study of brittle rock fracture in laboratory compression experiments. Int J Rock Mech Min Sci 1970;7:561–75.
[23] Amitrano D. Emission acoustique des roches et endommagement. Approches expérimentale et numérique—application à la seismicité minière [Ph.D. thesis]. Grenoble, France: Université Joseph Fourier; 1999.
[24] Fjaer E, Holt RM, Horsrud P, Raaen AM, Risnes R. Petroleum related rock mechanics. 2nd ed.. Amsterdam: Elsevier; 2008.
[25] Pettitt W, Young RP. InSite user operations manual. Shrewsbury, UK: Applied Seismology Consultants; 2007.
[26] Aki K, Richards PG. Quantitative seismology. Sausalito, Cailf: University Science Books; 2002.
[27] Sokos E, Zahradník J. ISOLA—a fortran code and matlab GUI to perform multiple point source inversion of seismic data. Comput Geosci 2008;34: 967–77.
[28] Vavryčuk V, Kühn D. Moment tensor inversion of waveforms: a two-step time-frequency approach. Geophys J Int 2012;190:1761–76.
[29] Menke W. Geophysical data analysis: discrete inverse theory. New York: Academic Press; 1989.
[30] Reches Z, Lockner DA. Nucleation and growth of faults in brittle rocks. J Geophys Res 1994;99(B9):18159–73.
[31] Katz O, Reches Z. Microfracturing, damage, and failure of brittle granites. J Geophys Res 2004;109:B01206.
[32] Stanchits S, Vinciguerra S, Dresen G. Ultrasonic velocities, acoustic emission characteristics and crack damage of basalt and granite. Pure Appl Geophys 2006;163:974–93.